Structural and Performance Relationships of Mechanochemically Synthesized Piezoelectric Catalysts $BaTiO_3$, $NaNbO_3$ and $BiFeO_3$

Supplemental Information

Erin V. Phillips[a], Van Son Nguyen,[b] Marta Hatzell[b,c], Carsten Sievers[a,c*]

[a]School of Chemistry and Biochemistry, Georgia Institute of Technology, Atlanta, GA 30332, United States

[b]School of Chemical & Biomolecular Engineering, Georgia Institute of Technology, Atlanta, GA 30332, United States

[c]George W. Woodruff School of Mechanical Engineering, Atlanta, GA 30318, United States

Email: carsten.sievers@chbe.gatech.edu

Number of Pages: 33

Number of Figures: 23

Number of Images: 18

Number of Schemes: 1

Number of Equations: 18

Section S1: Supplemental Results for Catalyst Characterization

S1.1: XRD

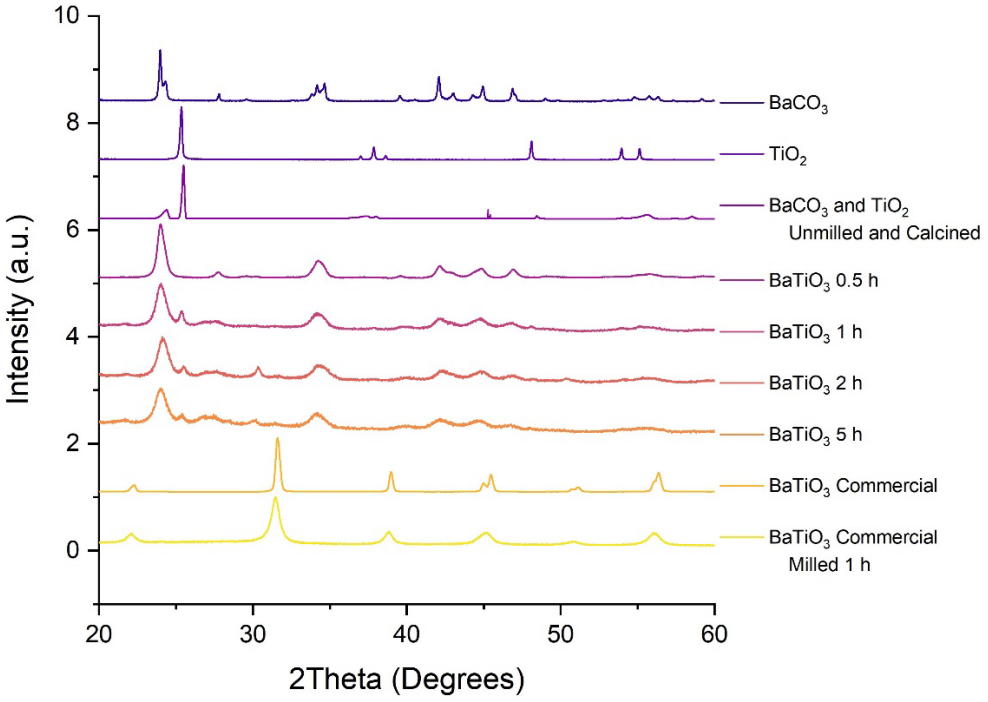

Figure S1: XRD of $BaTiO_3$ precursors $BaCO_3$ and TiO_2, commercial $BaTiO_3$ and milled $BaTiO_3$ before calcination from 20° to 70°.

Figure S1 demonstrates the necessity for milling followed by calcination to obtain a fully formed version of $BaTiO_3$. First, a combination of $BaCO_3$ and TiO_2 is shown, without any milling; the precursors were simply combined and mixed with a spatula, followed by a 45 min calcination at 800°C. Strong peak correlation to $BaCO_3$ and TiO_2 after calcination shows that heating alone was not sufficient to fuse $BaCO_3$ and TiO_2 into a singular phase of $BaTiO_3$. Next, the mechanochemically milled combinations are shown from 0.5 h to 5 h without heating. Before calcination, a strong peak correlation to $BaCO_3$ existed directly after milling, confirming that the calcination step was necessary to finish $BaTiO_3$ formation. Finally, commercial $BaTiO_3$ is shown after milling for 1 h at 30 Hz to demonstrate that both the commercial and mechanochemically synthesized catalysts adopted the same P_{m3m} cubic lattice over time.

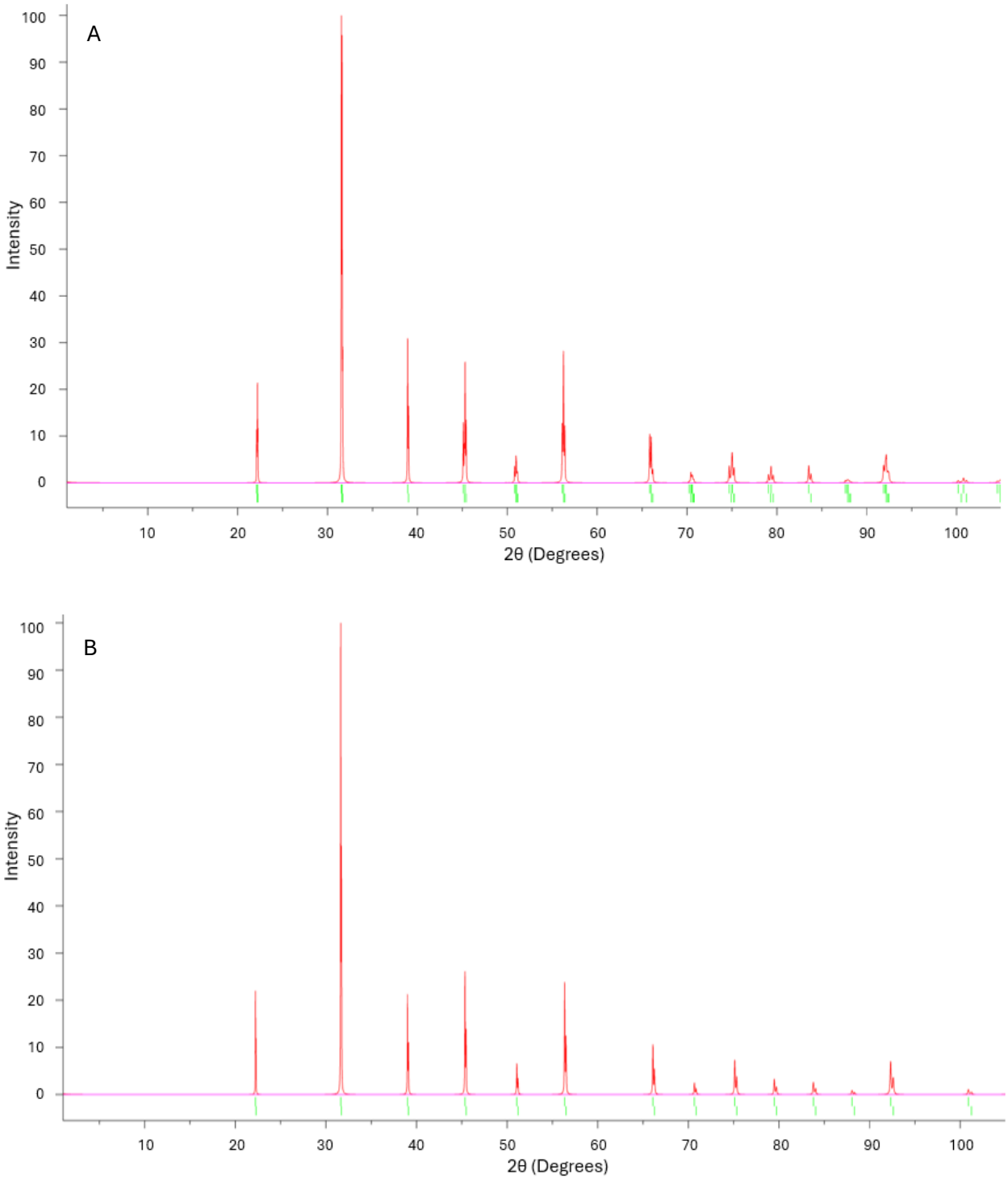

Figure S2: Reference XRD spectra used to determine $BaTiO_3$ phases obtained from the COD. (A)[1] P_{4mm} and (B)[2] P_{m3m}.

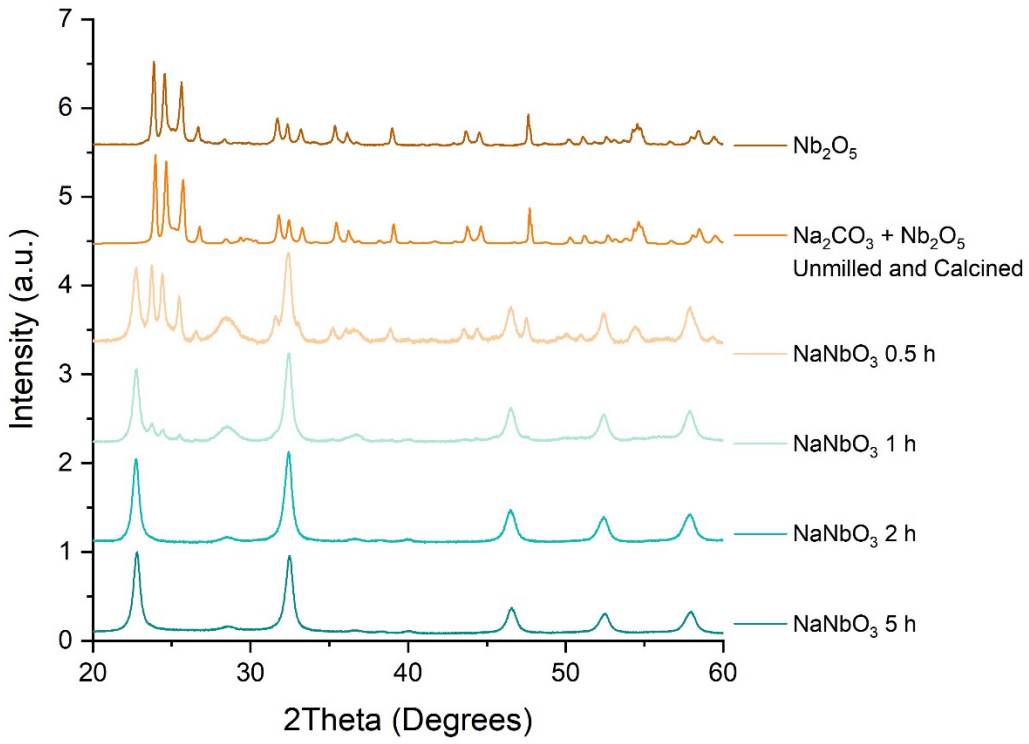

Figure S3: XRD of $NaNbO_3$ precursor Nb_2O_5, combined and calcined Na_2CO_3 and Nb_2O_5 and milled $NaNbO_3$ before calcination from 20° to 60°.

The graph depicted in Figure S3 shows a similar trend to Figure S1. When Na_2CO_3 and Nb_2O_5 were simply mixed and calcined (650°C for 2 h) without any milling, no formation of $NaNbO_3$ was apparent. A strong Nb_2O_5 presence dominated the diffractogram. Unlike $BaTiO_3$, when the two precursors were milled and not calcined, new peak formation correlating to $NaNbO_3$ did begin to occur. After 0.5 h of milling, a combination of Nb_2O_5 and $NaNbO_3$ was presented on the diffractogram, indicating a transition phase, which was reduced with 1 h of milling. After 2 h and up to 5 h, $NaNbO_3$ becomes the singular phase present. The arylation test reaction was initially conducted with non-calcined $NaNbO_3$, but a number of side reactions occurred. After calcining $NaNbO_3$, a clean product was obtained, suggesting that calcination was in fact necessary. Peak width reduced and intensity increased, indicating that a shift from an amorphous phase to a crystalline phase occurred with heating.

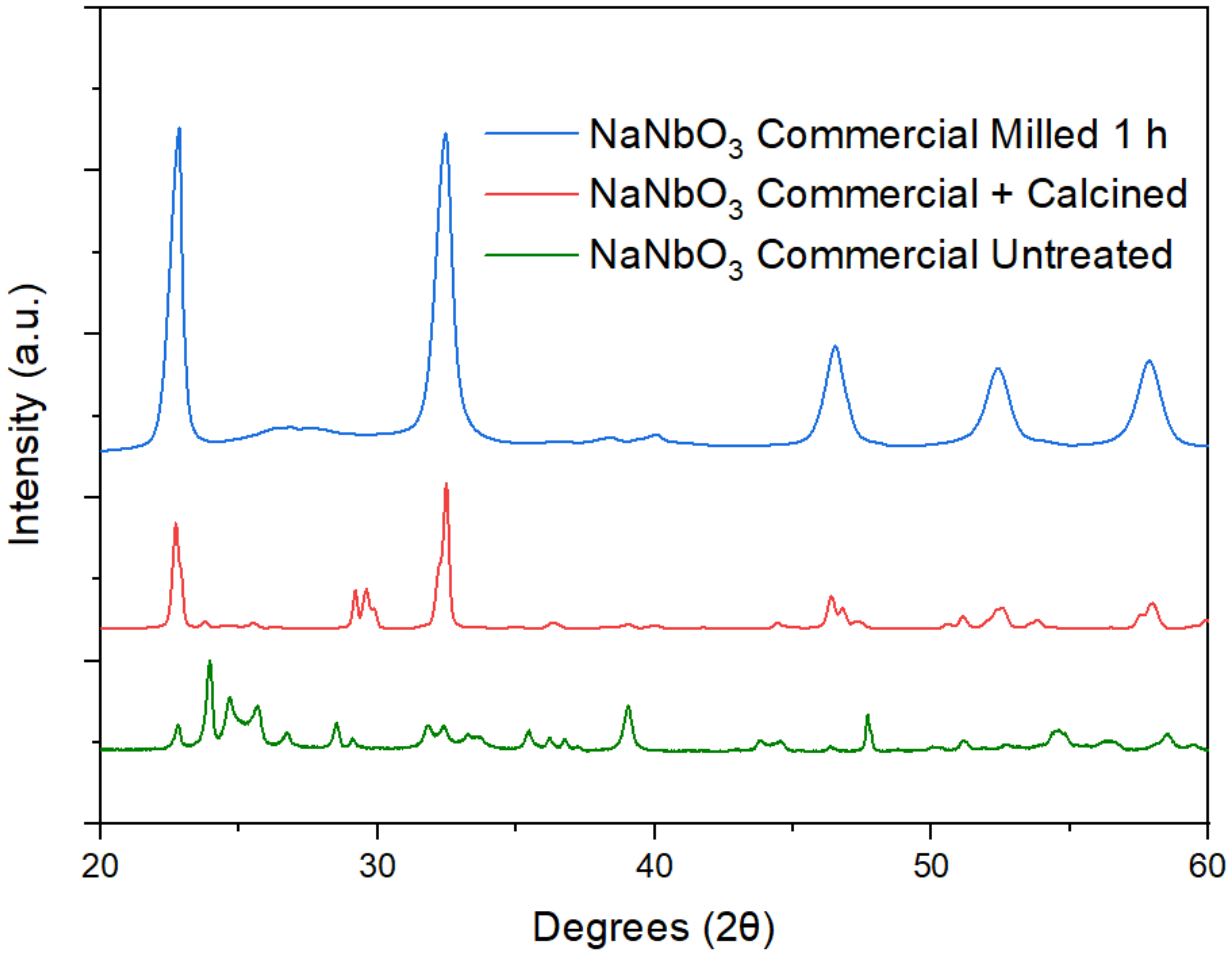

Figure S4: XRD of the fresh commercial $NaNbO_3$, after calcination and after 1 h of milling.

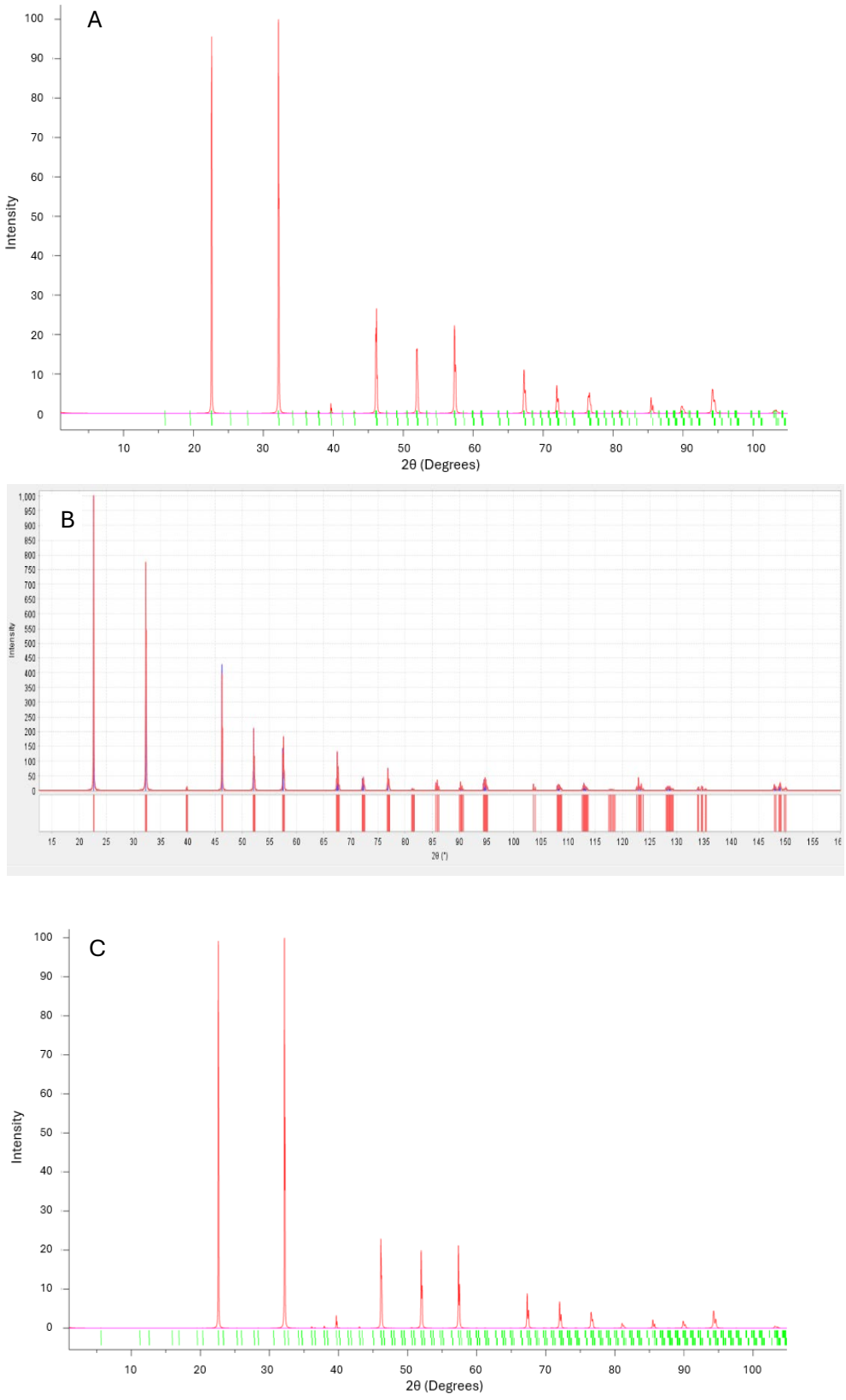

Figure S5: Reference XRD spectra used to determine $NaNbO_3$ phases and Miller indices obtained from the COD and PDF-2 Database. (A)[3] C_{cmm}, (B)[4] $P_{12/m1}$ and (C)[5] $P_{mmn:2}$.

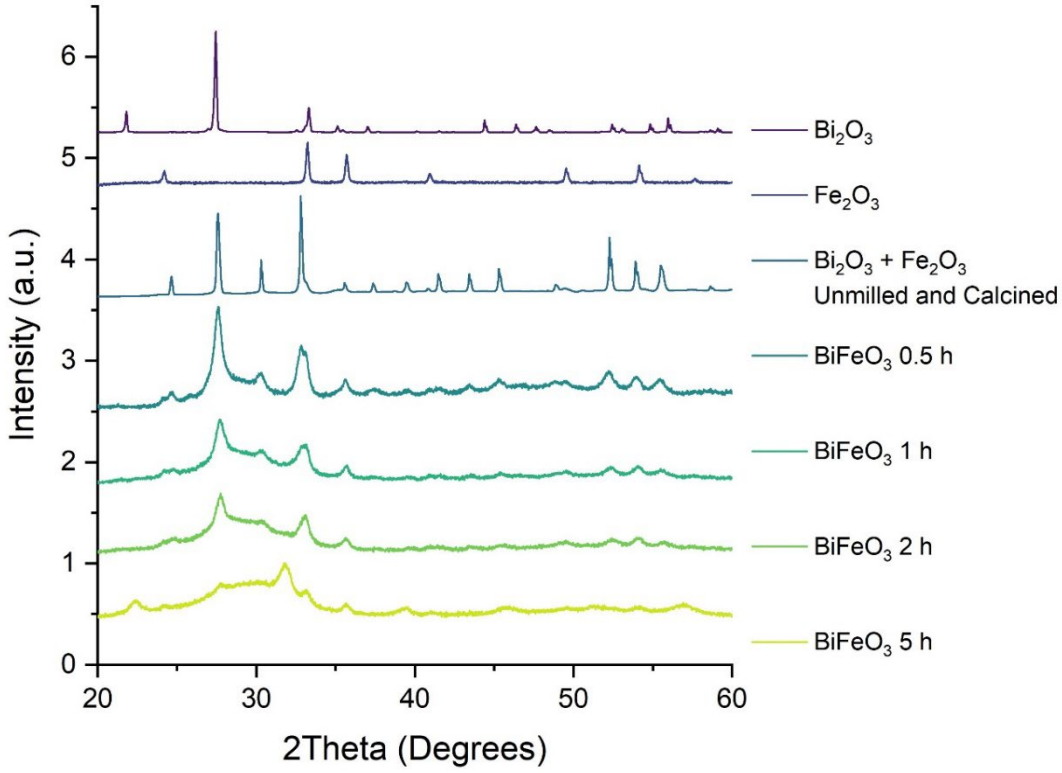

Figure S6: XRD of $BiFeO_3$ precursors Bi_2O_3 and Fe_2O_3, combined and calcined Bi_2O_3 and Fe_2O_3 and milled $BiFeO_3$ before calcination from 20° to 60°.

The calcination of Bi_2O_3 and Fe_2O_3 without milling showed that a slight phase change occurred with calcination only in Figure S6. The peaks at 30.3°, 39.4°, 43.4°, and 52.3° are significantly prominent, amongst additional minor peaks that present after calcination, but do not align with Bi_2O_3 or Fe_2O_3. Milling Bi_2O_3 and Fe_2O_3 without calcination showed a significant amount of amorphicity. The Bi_2O_3 peak at 27.4° remained present in the structure through 2 h of milling, along with the peak at 32.8°. The characteristic peaks for $BiFeO_3$ at 22.5° and 32° did not begin to appear until after 5 hours of milling. Similar to $BaTiO_3$ calcination caused a significant phase shift for $BiFeO_3$, fully eliminating any amorphous phases present in the milled sample. Figure S1, S3 and S6 demonstrate that calcination was necessary for all three catalysts to complete crystalline structure formation.

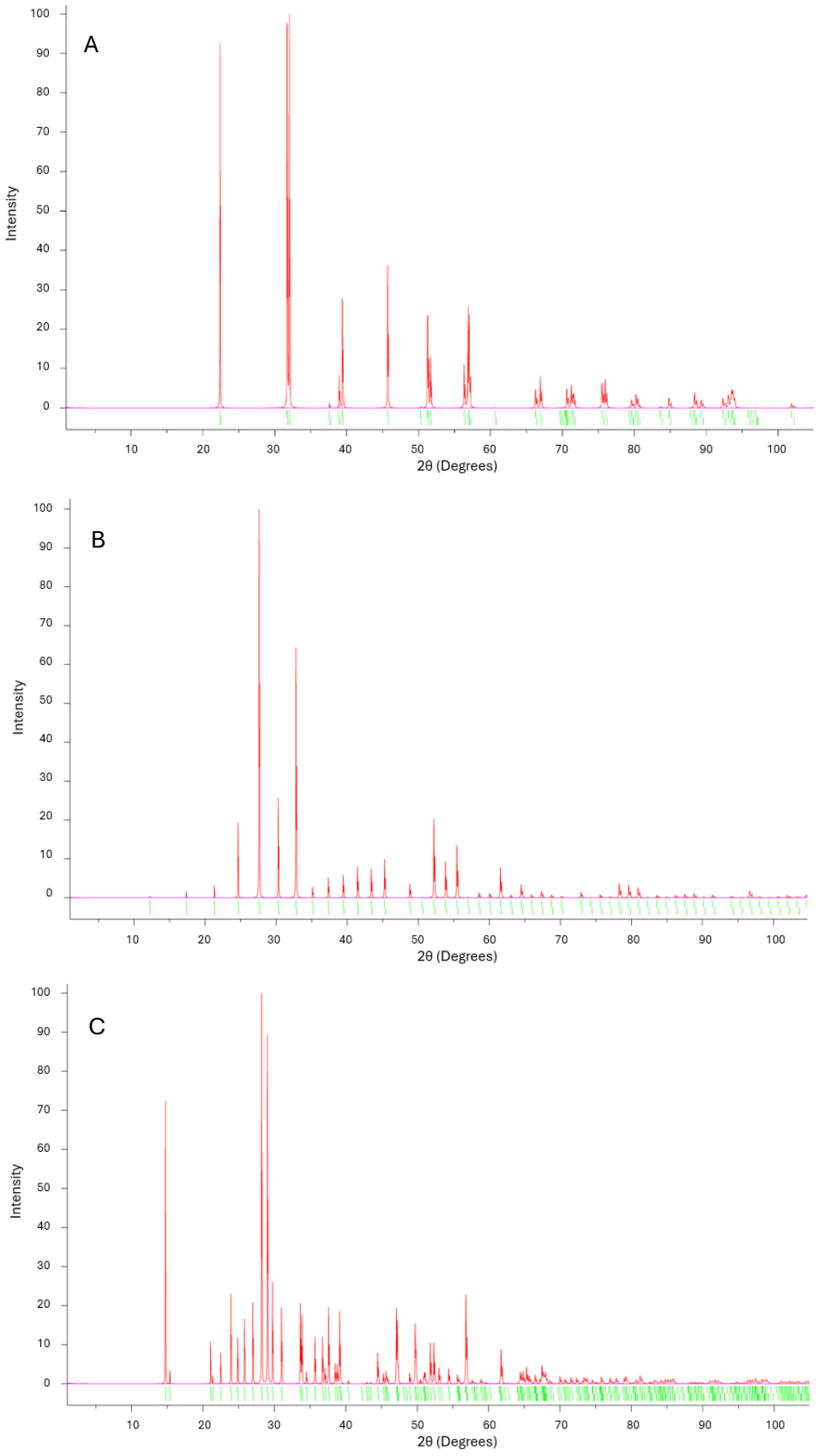

Figure S7: Reference XRD spectra used to determine $BiFeO_3$ phases and Miller indices obtained from the COD database. (A)[6] $R_{3c:H}$ ($BiFeO_3$), (B)[7] I_{23} ($Bi_{25}FeO_{39}$) and (C)[8] P_{bam} ($Bi_2Fe_4O_9$).

S1.2 N_2 Physisorption

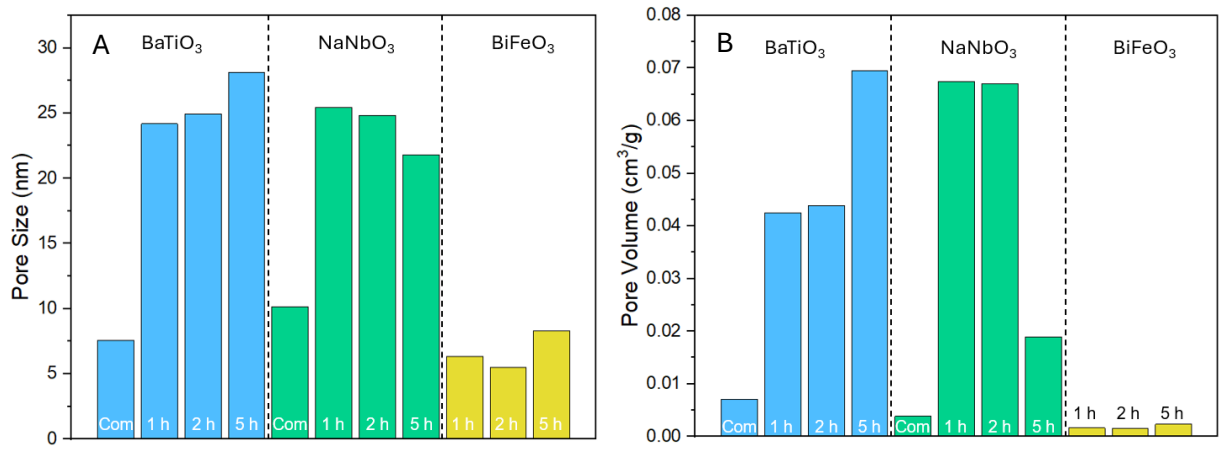

Figure S8: N_2 Physisorption results for the three catalysts. Pore volume (cm^3/g) (A) and pore diameter (nm) (B) are shown.

N_2 physisorption results for $BaTiO_3$, $NaNbO_3$ and $BiFeO_3$ pore diameter and pore volume are depicted in Figure S8. A similar behavior was observed for these two dimensions as what was depicted for surface area in Figure 3 of the main manuscript. Although the overall surface areas were low, porosity still played an important role in the reactivity of these catalysts. The pore diameter and volume for commercial $BaTiO_3$ and $NaNbO_3$ were much smaller than their mechanochemically synthesized counterparts. Significant differences were observed for pore volume specifically, where $BaTiO_3$ HM5C was 10 times greater than commercial $BaTiO_3$ and $NaNbO_3$ was nearly 20 times greater than commercial $NaNbO_3$. As previously mentioned, $BaTiO_3$ and $NaNbO_3$ maintained relatively stable parameters from 1 to 2 h of milling, but notable changes occurred after 5 h. For pore volume, $BaTiO_3$ increased by a factor of 1.6 from 2 to 5 h of milling, whereas $NaNbO_3$ decreased by a factor of 3.5. This suggested that $BaTiO_3$ was continuing to expose new surfaces and created larger exposed pores whereas $NaNbO_3$ began to degrade, and the structure likely began to collapse on itself, shrinking the pores. For particle diameter, more subtle changes were observed. $BaTiO_3$ increased by 3.2 nm from 2 to 5 h of milling, whereas $NaNbO_3$

decreased by 3.7 nm. These minimal changes further support the previous statement regarding pore volume; $BaTiO_3$ likely became more porous and had deeper cavities within the structure, whereas $NaNbO_3$ developed shallower pores, decreasing porosity. $BiFeO_3$ showed a steady pore volume throughout milling (0.002 cm^3/g) with a slight increase (2 nm) in pore diameter; this suggests that $BiFeO_3$ is also subject to pores becoming shallower. As the diameter increases, if pore volume is stagnant, this indicates that depth was being lost.

S 1.3 SEM

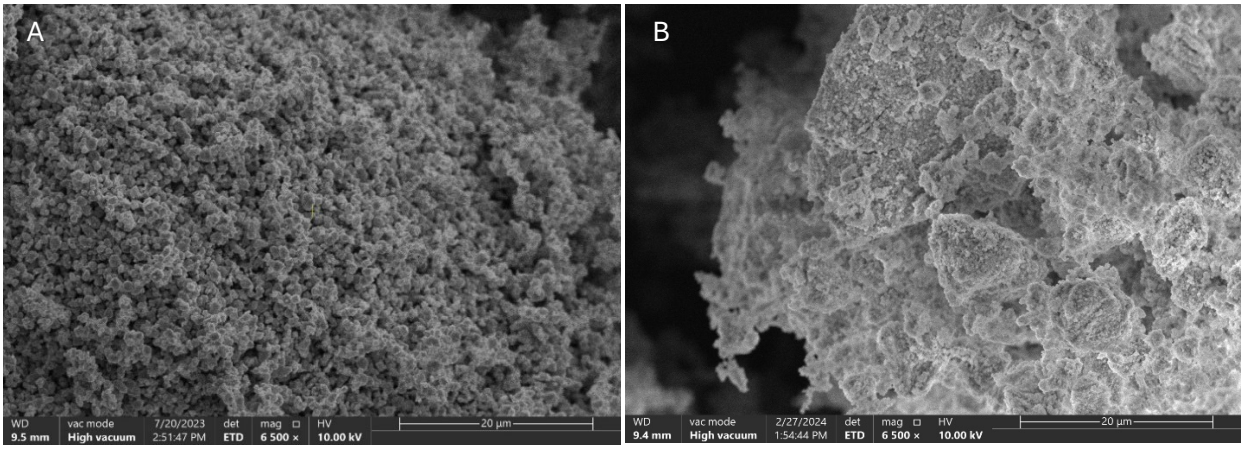

Figure S9: SEM images for commercial $BaTiO_3$ (left) and HM1C $BaTiO_3$ (right) at 20 µm.

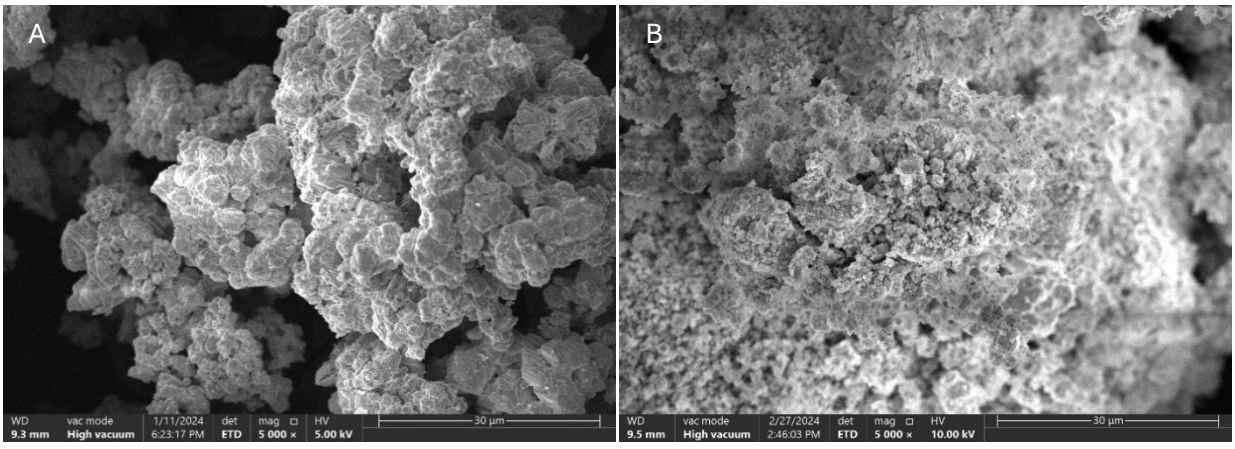

Figure S10: SEM images for commercial $NaNbO_3$ (left) and HM1C $NaNbO_3$ (right) at 30 µm.

For $BaTiO_3$ and $NaNbO_3$, the same transformations were observed through SEM imaging (Figure S9 and S10); the milled samples had much rougher surfaces with greater porosity and smaller particle size in comparison to the commercial samples. This further confirmed the trends seen by surface area and average particle size in Figures 3 and 4. The particle sizes of both $NaNbO_3$ samples and milled $BaTiO_3$ showed a large distribution of various particle sizes and shapes, whereas commercial $BaTiO_3$ had a more uniform, spherical structure. Apart from commercial $BaTiO_3$, the exact particle size is difficult to determine via SEM. For milled $BaTiO_3$ and $NaNbO_3$, Figures S9B and S10B demonstrate large, agglomerated particles, with much finer, lose particles spread across the surface. For commercial $NaNbO_3$ (Figure S10A), there is a lack of uniformity, so particle size cannot be determined visually. For this reason, milled $BaTiO_3$ and $NaNbO_3$ and commercial $NaNbO_3$ particle sizes are best understood through TEM image analysis.

S 1.4 TEM

Figures S11 – S16 depict TEM images and histograms of all commercial and mechanochemically synthesized catalysts (HM0.5C, HM1C, HM2C and HM5C) for $BaTiO_3$, $NaNbO_3$ and $BiFeO_3$. To elucidate differences in particle sizes, all images are shown at a 100 nm scale. As stated in the main text, mechanochemically synthesized $BaTiO_3$ (Figure S11) and $NaNbO_3$ (Figure S12) particles were significantly smaller than their commercial counterparts.

The TEM images of $BiFeO_3$ shown in Figure S13A and B examined single $BiFeO_3$ particles, roughly 250 nm in diameter. N_2 physisorption confirmed that $BiFeO_3$ particles overall were much larger than mechanochemically synthesized $BaTiO_3$ and $NaNbO_3$ particles, while the arylation test reaction showed that $BiFeO_3$ activity was inferior to the other two catalysts. Where $BaTiO_3$ and $NaNbO_3$ had extremely strong and clear parallel lattice plains, the crystalline sections for $BiFeO_3$ observed through TEM were comparatively weaker, but still observable.

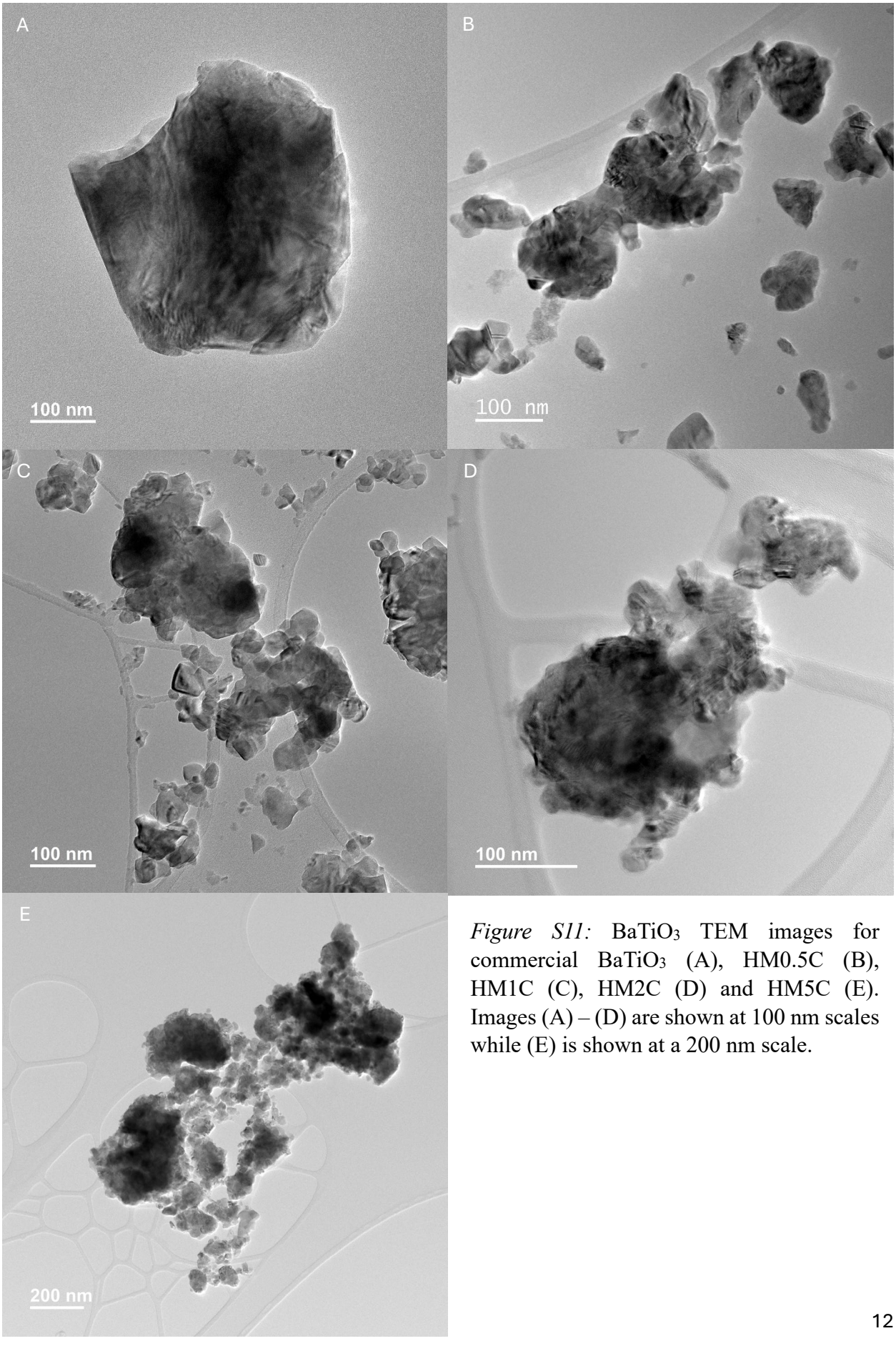

Figure S11: $BaTiO_3$ TEM images for commercial $BaTiO_3$ (A), HM0.5C (B), HM1C (C), HM2C (D) and HM5C (E). Images (A) – (D) are shown at 100 nm scales while (E) is shown at a 200 nm scale.

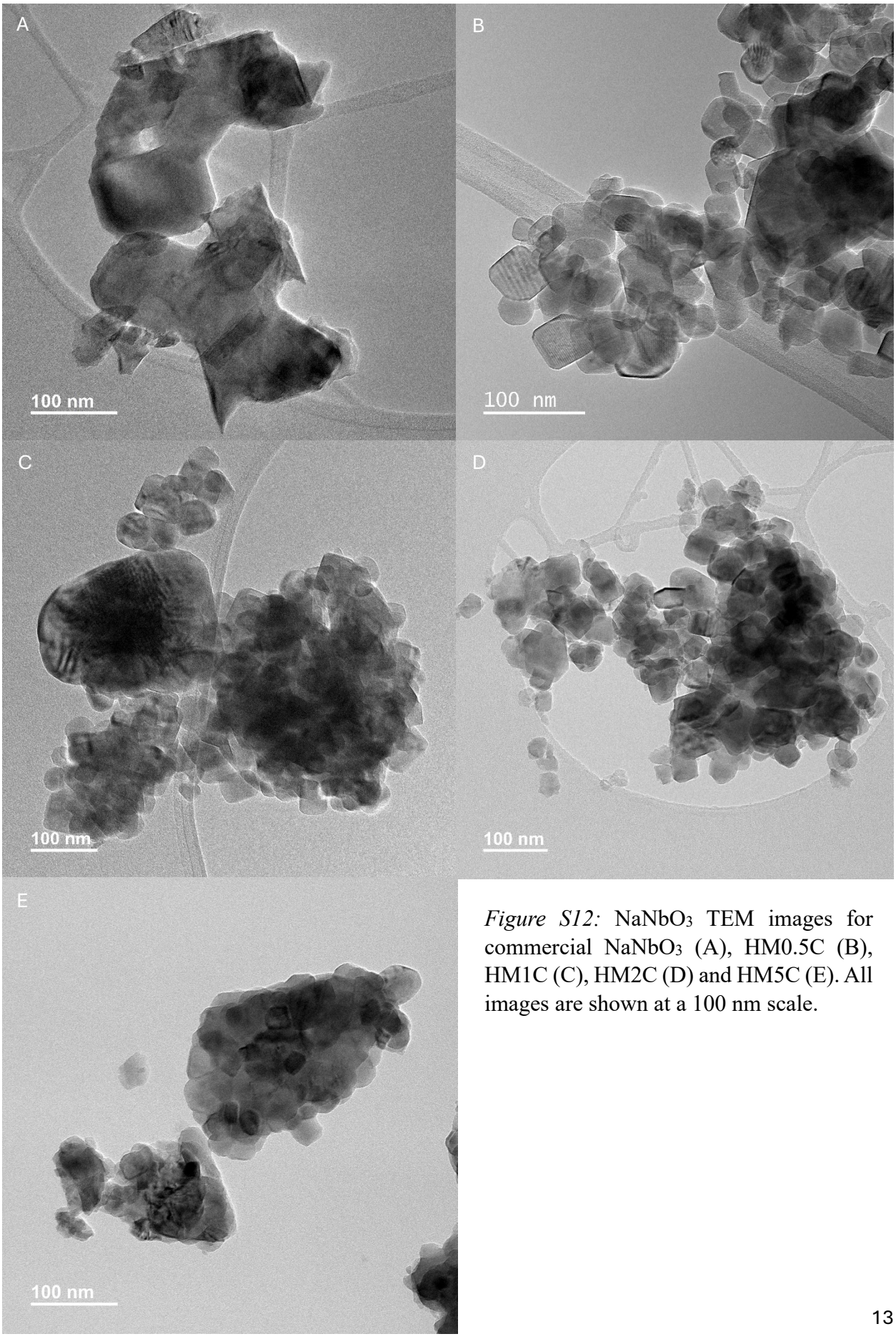

Figure S12: $NaNbO_3$ TEM images for commercial $NaNbO_3$ (A), HM0.5C (B), HM1C (C), HM2C (D) and HM5C (E). All images are shown at a 100 nm scale.

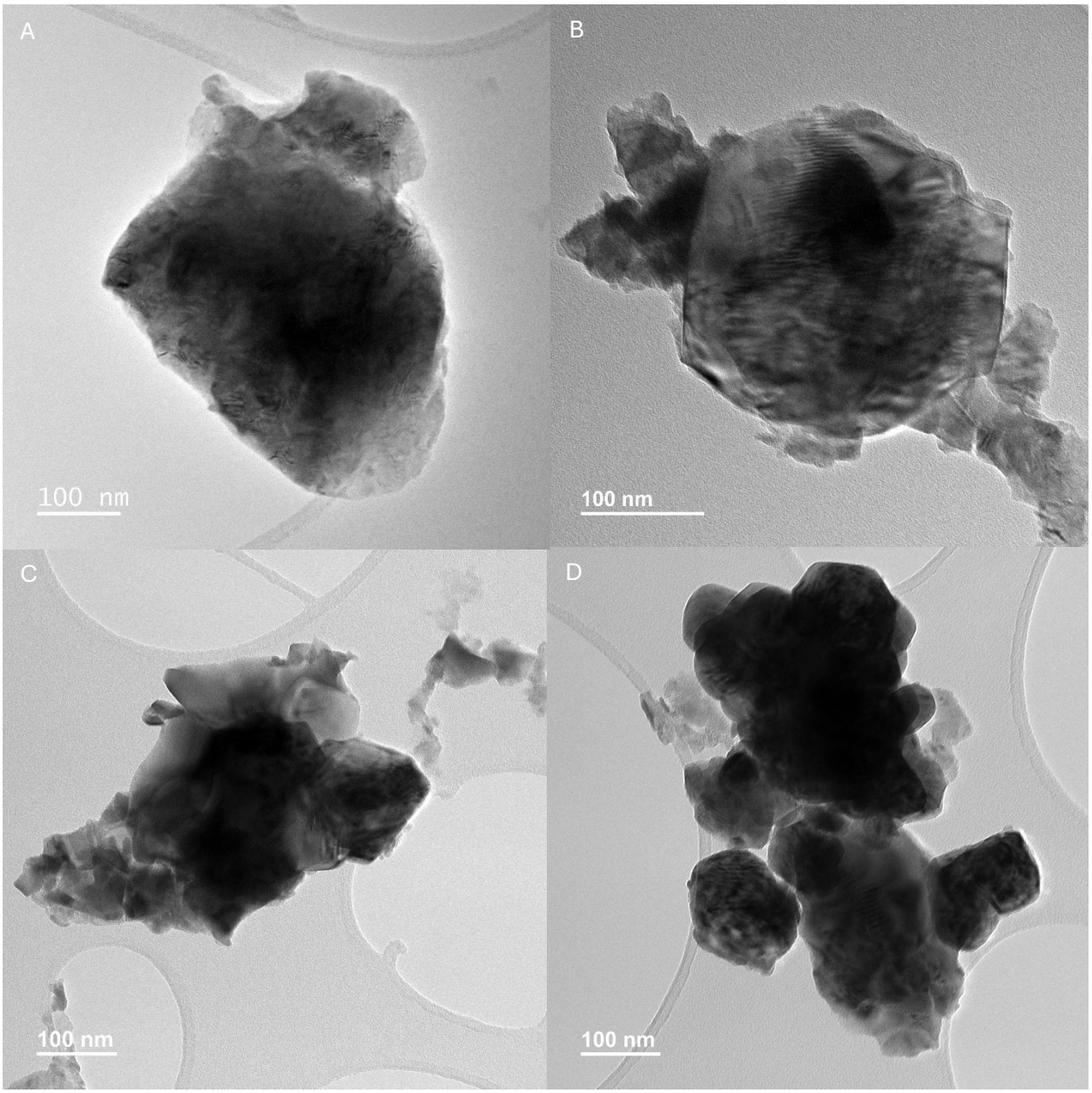

Figure S13: $BiFeO_3$ TEM images for HM0.5C (A), HM1C (B), HM2C (C) and HM5C (D). All images are shown at a 100 nm scale.

The weakened observable parallel lattice plains confirmed that $BiFeO_3$ (Figure S13) was less crystalline than $BaTiO_3$ and $NaNbO_3$, and therefore less conductive. With the contamination of $Bi_{25}FeO_{40}$ and $Bi_2Fe_4O_9$, the homogeneity of the material was compromised, and it became less effective when transferring electrical energy throughout the structure due to decreased piezoelectric properties and increased symmetric phase concentrations.

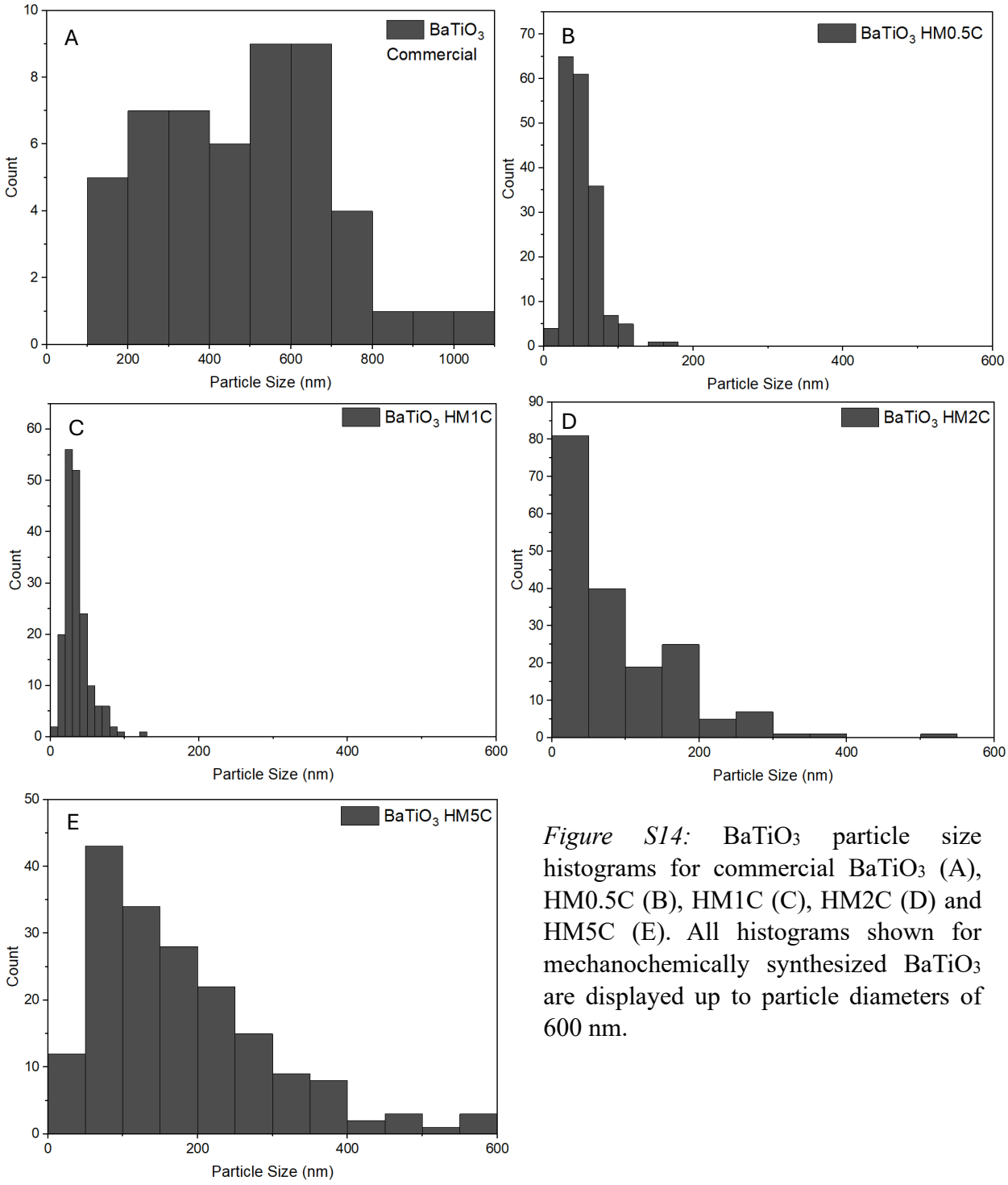

Figure S14: $BaTiO_3$ particle size histograms for commercial $BaTiO_3$ (A), HM0.5C (B), HM1C (C), HM2C (D) and HM5C (E). All histograms shown for mechanochemically synthesized $BaTiO_3$ are displayed up to particle diameters of 600 nm.

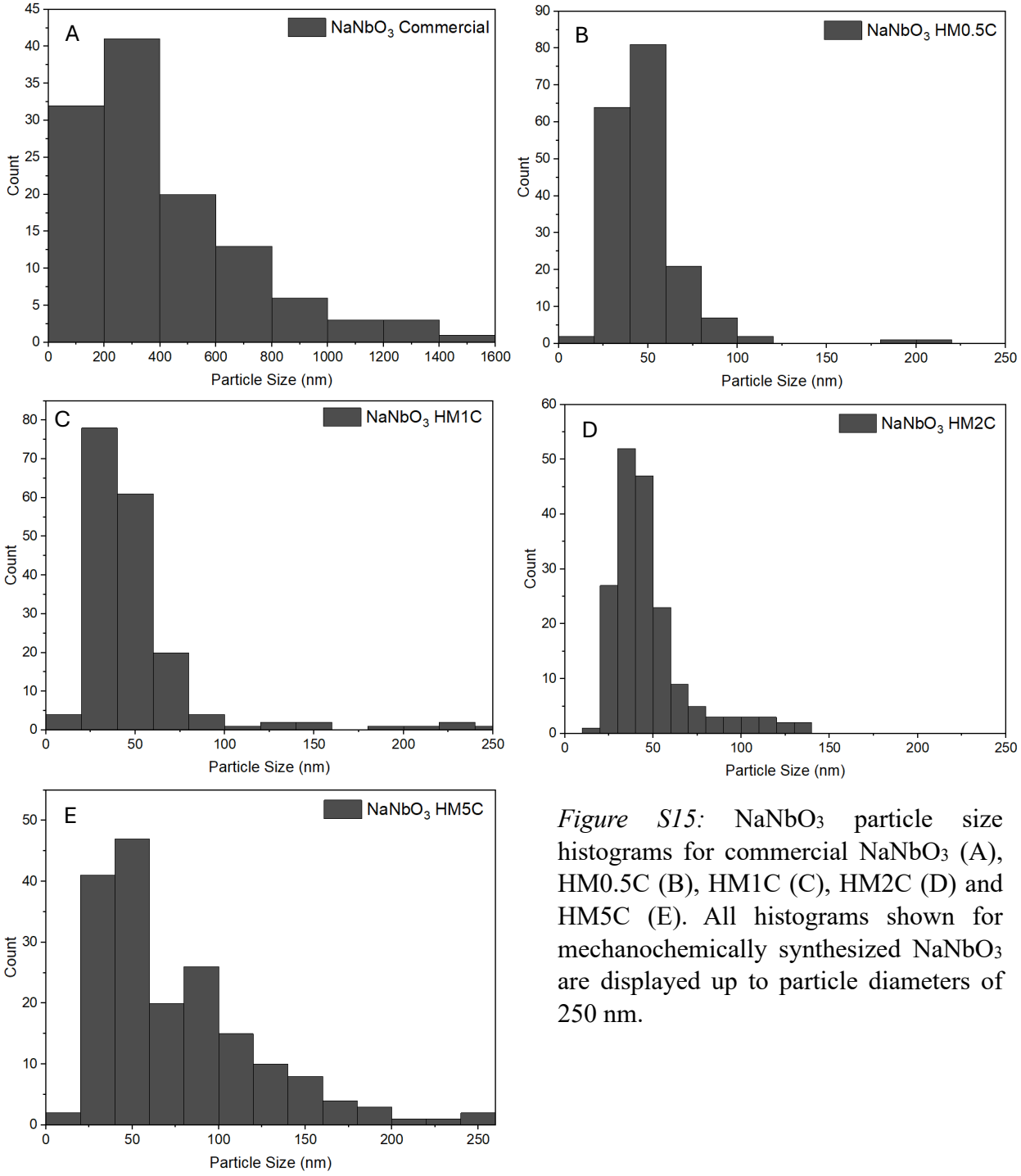

Figure S15: $NaNbO_3$ particle size histograms for commercial $NaNbO_3$ (A), HM0.5C (B), HM1C (C), HM2C (D) and HM5C (E). All histograms shown for mechanochemically synthesized $NaNbO_3$ are displayed up to particle diameters of 250 nm.

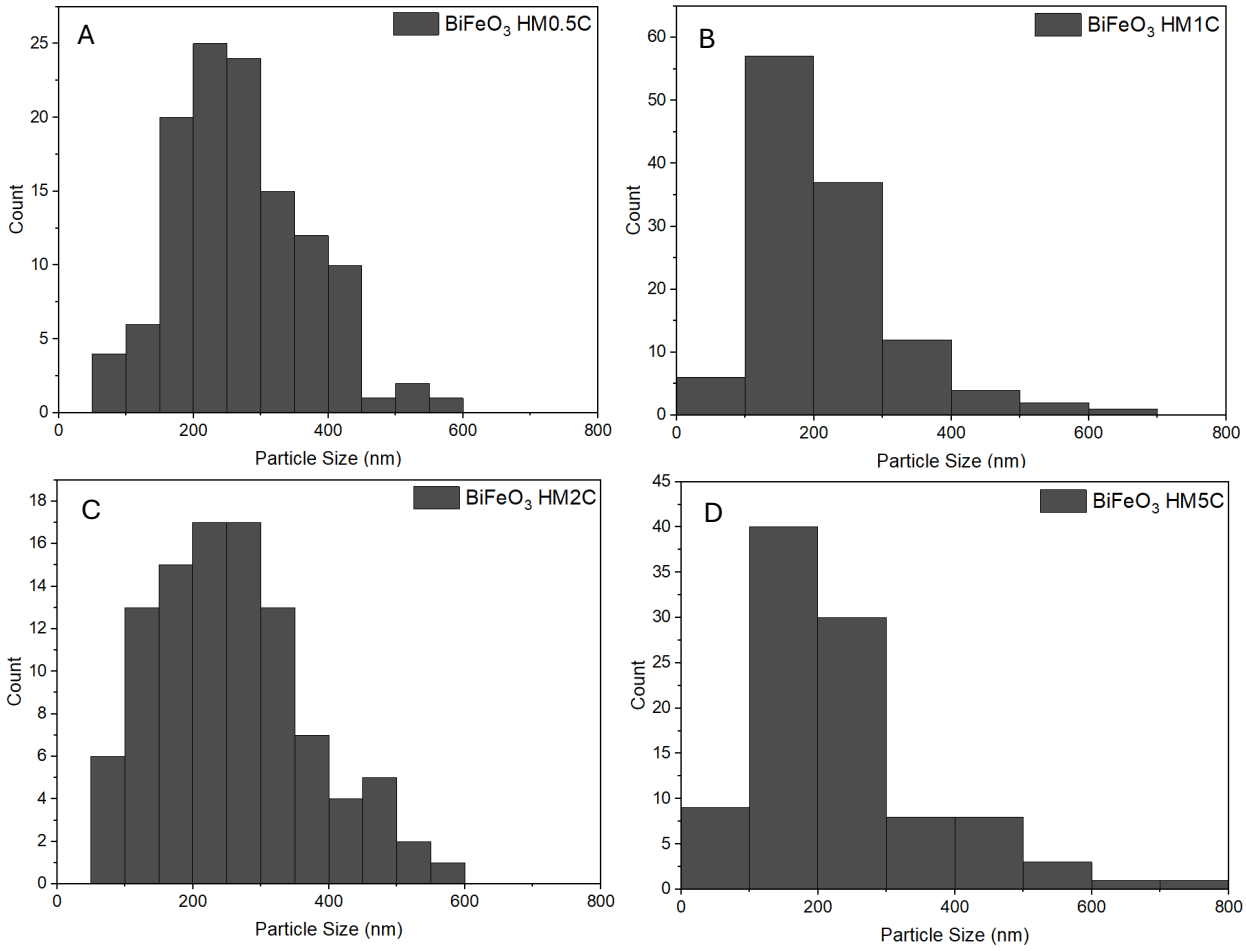

Figure S16: $BiFeO_3$ particle size histograms for HM0.5C (A), HM1C (B), HM2C (C) and HM5C (D). All histograms shown for mechanochemically synthesized $BiFeO_3$ are displayed up to particle diameters of 800 nm.

Section S2: Supplemental Results for Arylation Reaction

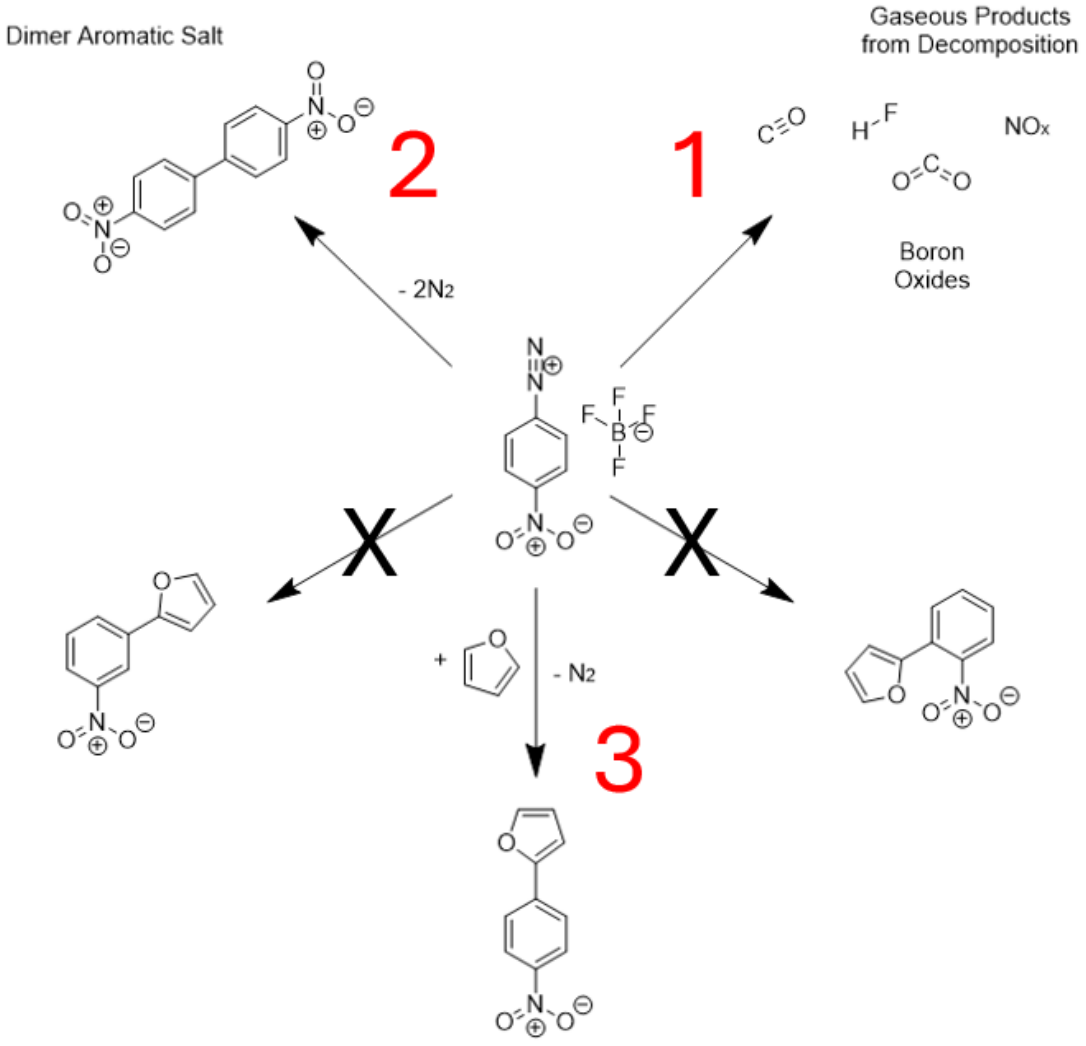

Scheme S1: Potential reaction pathways for the arylation of 4-nitrobenzenediazonium tetrafluoroborate and furan when milled under atmospheric conditions.

Scheme S1 shows the three potential pathways for the arylation reaction of 4-nitrobenzenediazonium tetrafluoroborate and furan. Pathway 1 is discussed in section 3.3 of the manuscript, where the diazonium salt is decomposed to its basic components, mainly CO, CO_2, NO_x gases, boron oxides and gaseous HF, resulting in 30% feedstock loss, based solely off mechanochemical heat impact. Pathways 2 and 3 are explained by ^{1}H NMR findings and kinetics.

S2.1 Kinetics and Material Behaviors

The general rate expression can be derived from the reaction sequence with several simplifying assumptions in the analysis summed up as follows:

1. The protonation step of 2-(4-nitrophenyl) furan with HBF_4 is assumed to be in quasi-equilibrium, meaning that the forward and reverse rates are equal ($r_5 = r_{-5}$). This gives the equilibrium constant K_5 defined as:

$$K_5 = \frac{k_5}{k_{-5}} = \frac{[O_2NPhC_4H_4O][HBF_4]}{[O_2NPhC_4H_4O^+][BF_4^-]} \quad \text{(SEQ1)}$$

2. Since the radicals are highly reactive and short-lived, the pseudo-steady-state hypothesis (PSSH) is applied to both the nitrophenyl ($(O_2NPh)^\bullet$) and the 2-(4-nitrophenyl) furan radicals ($O_2NPhC_4H_4O^\bullet$), meaning their concentrations are assumed to remain constant over time:

$$\frac{d}{dt}[(O_2NPh)^\bullet] = \frac{d}{dt}[O_2NPhC_4H_4O^\bullet] = 0 \quad \text{(SEQ2)}$$

3. The concentration of furan was in large excess relative to 4-nitrobenzenediazonium tetrafluoroborate, which implies that the order with respect to furan in Reaction R3 is zero, simplifying the rate expression:

$$r_3 = k_3[(O_2NPh)^\bullet] \quad \text{(SEQ3)}$$

From the quasi-equilibrium assumption of Reaction R5, we have:

$$\frac{d}{dt}[O_2NPhC_4H_4O^+] = \frac{d}{dt}[O_2NPhC_4H_4O] \quad \text{(SEQ4)}$$

For $BaTiO_3$ the first-order behavior of the rate of formation for both 2-(4-nitrophenyl) furan and 4,4'-dinitrobiphenyl relative to the mass of 4-nitrobenzenediazonium tetrafluoroborate can be explained as follows. From the PSSH illustrated in SEQ2, the rate of change relative to the concentration of $(O_2NPh)^{\bullet}$is given by:

$$\begin{aligned}\frac{d}{dt}[(O_2NPh)^{\bullet}] &= 0 \\ &= k_2[(O_2NPhN_2)^+BF_4^-][e^-] - k_3[(O_2NPh)^{\bullet}] \\ &\quad - k_6[(O_2NPh)^{\bullet}]^2 \qquad \text{(SEQ5)}\end{aligned}$$

$$k_2[(O_2NPhN_2)^+BF_4^-][e^-] = k_3[(O_2NPh)^{\bullet}] + k_6[(O_2NPh)^{\bullet}]^2$$

$$[(O_2NPh)^{\bullet}] = \frac{k_2[(O_2NPhN_2)^+BF_4^-][e^-]}{k_3 + k_6[(O_2NPh)^{\bullet}]}$$

Assuming a very low concentration of $(O_2NPh)^{\bullet}$, meaning that $k_6[(O_2NPh)^{\bullet}] \ll k_3$, $[(O_2NPh)^{\bullet}]$ can be approximated as:

$$[(O_2NPh)^{\bullet}] \approx \frac{k_2[(O_2NPhN_2)^+BF_4^-][e^-]}{k_3} \qquad \text{(SEQ6)}$$

Applying PSSH to $O_2NPhC_4H_4O^{\bullet}$, the concentration of 2-(4-nitrophenyl) furan radical is thus given as:

$$\begin{aligned}[O_2NPhC_4H_4O^{\bullet}] &= \frac{k_3[(O_2NPh)^{\bullet}]}{k_4[h^+]} = \frac{k_3}{k_4[h^+]}\frac{k_2[(O_2NPhN_2)^+BF_4^-][e^-]}{k_3} \\ &= \frac{k_2[(O_2NPhN_2)^+BF_4^-][e^-]}{k_4[h^+]} \qquad \text{(SEQ7)}\end{aligned}$$

The strength of the electric field E in a piezoelectric material is based on the piezoelectric charge coefficient d and the mechanical stress σ as well as the dielectric constant (or relative permittivity) ε:

$$E = \frac{d\sigma}{\varepsilon} \tag{SEQ8}$$

The concentration of electrons and holes is material-specific and proportional to E:

$$[\mathrm{e^-}] = [\mathrm{h^+}] \propto \mathrm{E} \propto \mathrm{k_{Mat}^*} \tag{SEQ9}$$

Thus, the concentration of the electron can be said to be specific to each material k_{Mat}^*. Using this, the rate of formation of 2-(4-nitrophenyl) furan ($\mathrm{r_{O_2NPhC_4H_4O}}$) is thus given by:

$$\begin{aligned}
\mathrm{r_{O_2NPhC_4H_4O,BaTiO_3}} &= \frac{\mathrm{d}}{\mathrm{dt}}[\mathrm{O_2NPhC_4H_4O^+}] = \frac{\mathrm{d}}{\mathrm{dt}}[\mathrm{O_2NPhC_4H_4O}] \\
&= \mathrm{k_4}[\mathrm{O_2NPhC_4H_4O^\bullet}][\mathrm{h^+}] = \mathrm{k_4}\frac{\mathrm{k_2}[(\mathrm{O_2NPhN_2})^+\mathrm{BF_4}^-][\mathrm{e^-}]}{\mathrm{k_4}}[\mathrm{h^+}] \\
&= (\mathrm{k_2 k_{BaTiO_3}^{*\,2}})[(\mathrm{O_2NPhN_2})^+\mathrm{BF_4}^-] \\
&= \mathrm{k_{C,BaTiO_{3,app}}}[(\mathrm{O_2NPhN_2})^+\mathrm{BF_4}^-]
\end{aligned} \tag{SEQ10}$$

As the concentration of the radical $(\mathrm{O_2NPh})^\bullet$ is small and lies close to 0, the value of $[(\mathrm{O_2NPh})^\bullet]^2$ can lie approximately close to $[(\mathrm{O_2NPh})^\bullet]$, which yields the same order for both reaction as observed. Thus, the rate expression for the formation of 4,4'-dinitrobiphenyl ($\mathrm{r_{(O_2NPh)_2}}$) can be approximated as:

$$
\begin{aligned}
r_{(O_2NPh)_2,BaTiO_3} &= k_6[(O_2NPh)^{\bullet}]^2 \approx k_6[(O_2NPh)^{\bullet}] \\
&= k_6 \frac{k_2[(O_2NPhN_2)^+BF_4^-][e^-]}{k_3} \\
&= \left(\frac{k_2 k_6 k^*_{BaTiO_3}}{k_3}\right)[(O_2NPhN_2)^+BF_4^-] \\
&= k_{E,BaTiO_{3,app}}[(O_2NPhN_2)^+BF_4^-]
\end{aligned}
\qquad \text{(SEQ11)}
$$

The observed rates therefore are both first order in relation to the mass of 4-nitrobenzenediazonium tetrafluoroborate for $BaTiO_3$.

In contrast, the zero-order behavior of the formation rates of both 2-(4-nitrophenyl) furan and 4,4'-dinitrobiphenyl for $NaNbO_3$ can be attributed to the relative reaction rates. Specifically, when the electron generation rate in R1 is significantly lower than the reaction rate of R2, R3, and R6 ($r_3 \gg r_1$, $r_6 \gg r_1$, $r_2 \gg r_1$). This suggests that the reaction rate is primarily dependent on the generation of electron-hole pairs in the piezoelectric catalyst and not on the mass of the diazonium salt. This observation implies that reaction R1 with a constant reaction rate is most likely to be the rate limiting step, which gives a zero-order dependence for both rate expressions:

$$r_{O_2NPhC_4H_4O,NaNbO_3} \propto r_1 \approx k_{C,NaNbO_3} k^*_{NaNbO_3} = k_{C,NaNbO_3,app} \qquad \text{(SEQ12)}$$

$$r_{(O_2NPh)_2,NaNbO_3} \propto {r_1}^2 \approx k_{E,NaNbO_3} {k^*_{NaNbO_3}}^2 = k_{E,NaNbO_3,app} \qquad \text{(SEQ13)}$$

With $BiFeO_3$, the half- and pseudo first-order behavior of the rate of formation for 2-(4-nitrophenyl) furan and 4,4'-dinitrobiphenyl, respectively, relative to the mass of 4-nitrobenzenediazonium tetrafluoroborate can be explained as follows. From the PSSH illustrated in SEQ2, $[(O_2NPh)^{\bullet}]$ can be determined as follows:

$$k_6[(O_2NPh)^{\bullet}]^2 + k_3[(O_2NPh)^{\bullet}] - k_2[(O_2NPhN_2)^{+}BF_4^{-}][e^{-}] = 0$$

$$[(O_2NPh)^{\bullet}] = \frac{-k_3 + \sqrt{k_3^2 + 4k_2k_6[(O_2NPhN_2)^{+}BF_4^{-}][e^{-}]}}{2k_6} \quad \text{(SEQ14)}$$

Here we can assume that the generation and the consumption of electron-hole pairs is in equilibrium as well as the dominance of the term under the square root, as the bandgap of $BiFeO_3$ is relatively low compared to the other catalysts (Figure 15B), thus, $[(O_2NPh)^{\bullet}]$can be approximated as:

$$[(O_2NPh)^{\bullet}] \approx \sqrt{\frac{k_2[(O_2NPhN_2)^{+}BF_4^{-}][e^{-}]}{k_6}} \quad \text{(SEQ15)}$$

Applying PSSH to $O_2NPhC_4H_4O^{\bullet}$, the concentration of the 2-(4-nitrophenyl) furan radical is thus given as:

$$[O_2NPhC_4H_4O^{\bullet}] = \frac{k_3[(O_2NPh)^{\bullet}]}{k_4[h^{+}]} = \frac{k_3}{k_4[h^{+}]}\sqrt{\frac{k_2[(O_2NPhN_2)^{+}BF_4^{-}][e^{-}]}{k_6}} \quad \text{(SEQ16)}$$

The expression of $r_{O_2NPhC_4H_4O,BiFeO_3}$ is thus described as:

$$\begin{aligned} r_{O_2NPhC_4H_4O,BiFeO_3} &= \frac{d}{dt}[O_2NPhC_4H_4O^+] = \frac{d}{dt}[O_2NPhC_4H_4O] \\ &= k_4[O_2NPhC_4H_4O^\bullet][h^+] \\ &= k_4 \frac{k_3}{k_4[h^+]} \sqrt{\frac{k_2[(O_2NPhN_2)^+BF_4^-][e^-]}{k_6}}\,[h^+] \\ &= k_3 \sqrt{\frac{k_2[(O_2NPhN_2)^+BF_4^-][e^-]}{k_6}} \\ &= \left(k_2^{\frac{1}{2}} k_3 k_6^{-\frac{1}{2}} [e^-]^{\frac{1}{2}}\right)[(O_2NPhN_2)^+BF_4^-]^{\frac{1}{2}} \\ &= \left(k_2^{1/2} k_3 k_6^{-1/2} {k^*_{BiFeO_3}}^{1/2}\right)[(O_2NPhN_2)^+BF_4^-]^{1/2} \\ &= k_{C,BiFeO_3,app}[(O_2NPhN_2)^+BF_4^-]^{1/2} \end{aligned} \quad \text{(SEQ17)}$$

Similarly, the expression of $r_{(O_2NPh)_2,BiFeO_3}$ is thus given by:

$$\begin{aligned} r_{(O_2NPh)_2,BiFeO_3} &= k_6[(O_2NPh)^\bullet]^2 = k_6 \frac{k_2[(O_2NPhN_2)^+BF_4^-][e^-]}{k_6} \\ &= k_2[(O_2NPhN_2)^+BF_4^-][e^-] = \left(k_2 k^*_{BiFeO_3}\right)[(O_2NPhN_2)^+BF_4^-] \\ &= k_{E,BiFeO_3,app}[(O_2NPhN_2)^+BF_4^-] \end{aligned} \quad \text{(SEQ18)}$$

The values for all the apparent reaction constants (k_{app}) are given in Figure 10C and 10E. The calculated yield compared to the measured yield of 2-(4-nitrophenyl) furan and 4,4'-dinitrobiphenyl shows good estimation of the reaction rate for all three catalysts (Figure 10B and 10D).

S 2.2 NMR

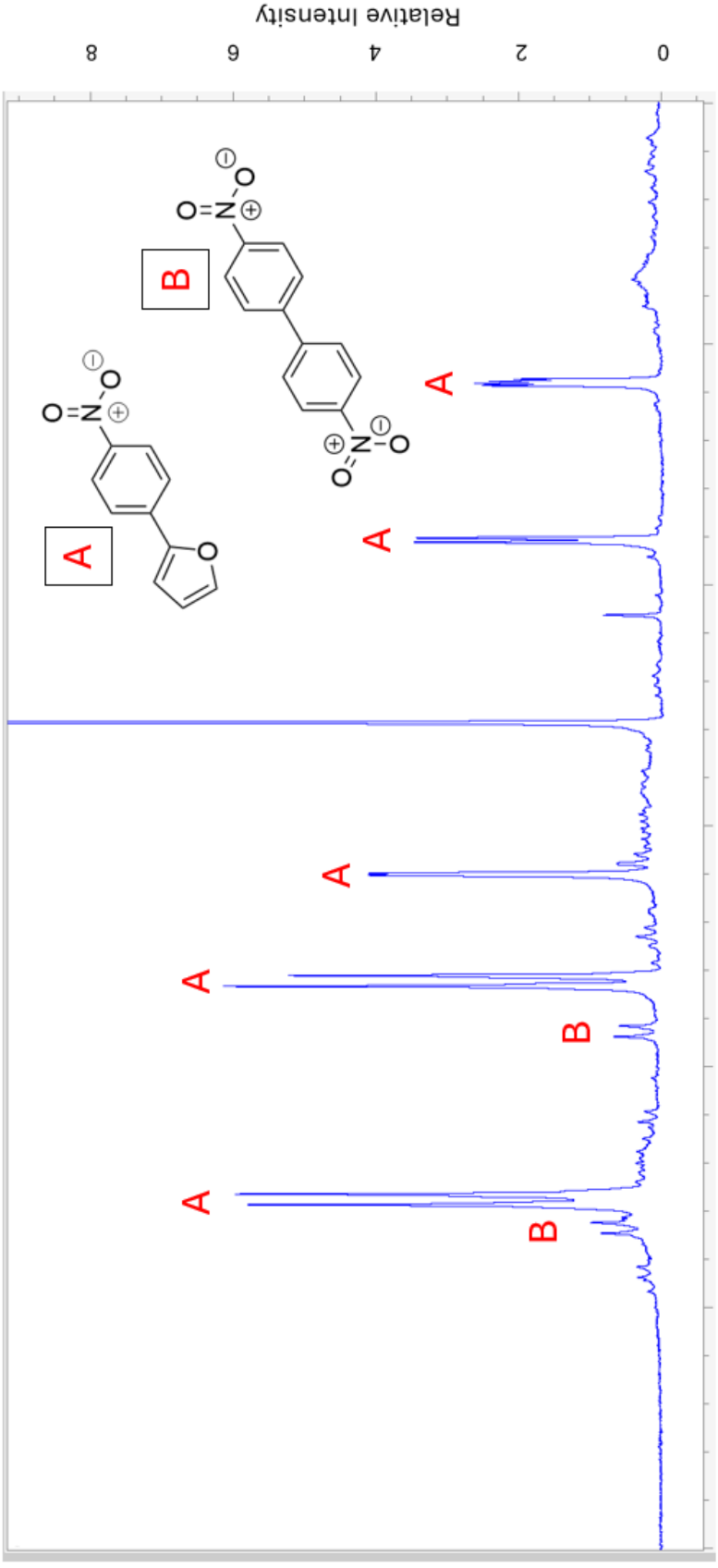

Figure S17: ^{1}H NMR spectrum of products from the arylation reaction using $NaNbO_3$ HM2C, which was the most optimal catalyst and produced the highest yield of 2-(4-nitrophenyl) furan at 44%.

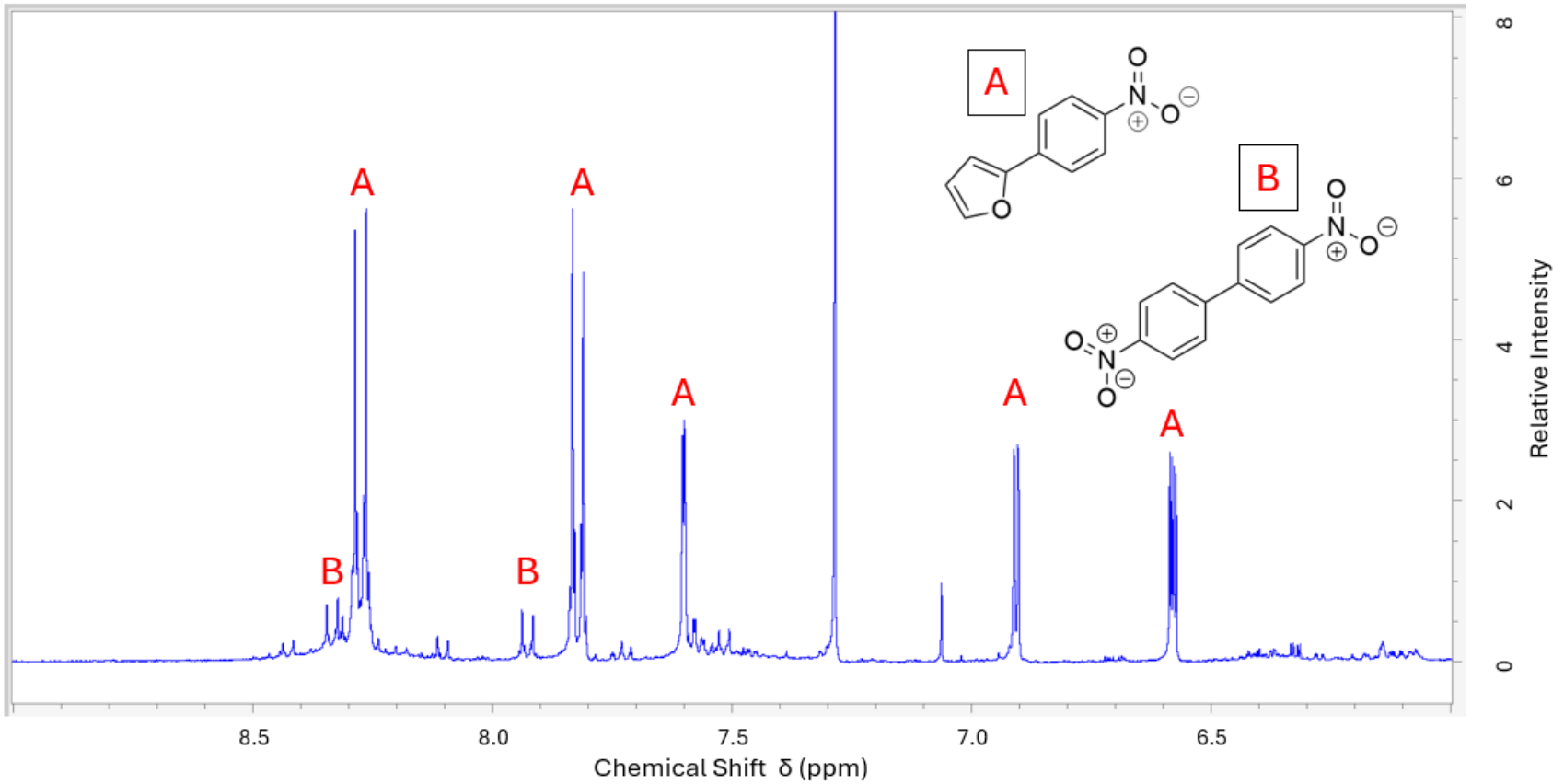

Figure S18: ^{1}H NMR spectrum of products from the arylation reaction using $BaTiO_3$ HM1C, which was the second best catalyst and produced a yield of 40% 2-(4-nitrophenyl) furan.

Figure S17 – S20 highlight the presence of the aromatic dimer as a consistent side product for this reaction. Figure S17 shows the experimental ^{1}H NMR spectra of $NaNbO_3$ HM2C after the arylation reaction; the crude mixture was dissolved in $CDCl_3$, sonicated and centrifuged before analysis. Figure S18 shows the spectra for $BaTiO_3$ HM1C after the arylation reaction. Figure S19 shows the ^{1}H NMR spectra for the 2-(4-nitrophenyl) furan standard. Figure S20 shows the resulting ^{1}H NMR spectra for the 4,4'-dinitrobiphenyl dimer, which resulted in two doublets, one at 7.82 ppm and one at 8.39 ppm. These same peaks appeared in all spectra for all three catalysts consistently, confirming that this side reaction definitively occurred, after the removal of the N_2 group from the salt feedstock.

To rule out other potential pathways of nitrophenyl furan formation, the ortho and meta isomers were also considered based on comparison with the reference spectra published by Hari et. al.[9] (Figure S21). For the ortho isomer, a double doublet at 6.7 ppm and a double triplet at 7.4 ppm would be observed, but these features were not present in the experimental spectra (Figure S17 and S18). For the meta isomer, there is a multiplet present at 8.5 ppm, which was also not observed. This ultimately suggests that when the reaction is successful, 100% selectivity to the desired para position occurs. When looking at the experimental spectra for the arylation reaction (Figure S17 and S18), it can be confirmed that no other significant side reactions are occurring besides decomposition and dimer formation.

It is important to note that it is a common practice in kinetic studies to hypothesize reaction mechanisms and potential pathways and probe whether they can accurately predict the observed measurable data. It is recognized that this approach cannot definitively confirm every potential pathway of the specific reaction mechanism depicted in Scheme S1 beyond doubt, but it can establish plausibility or allow for disproving incorrect hypotheses.

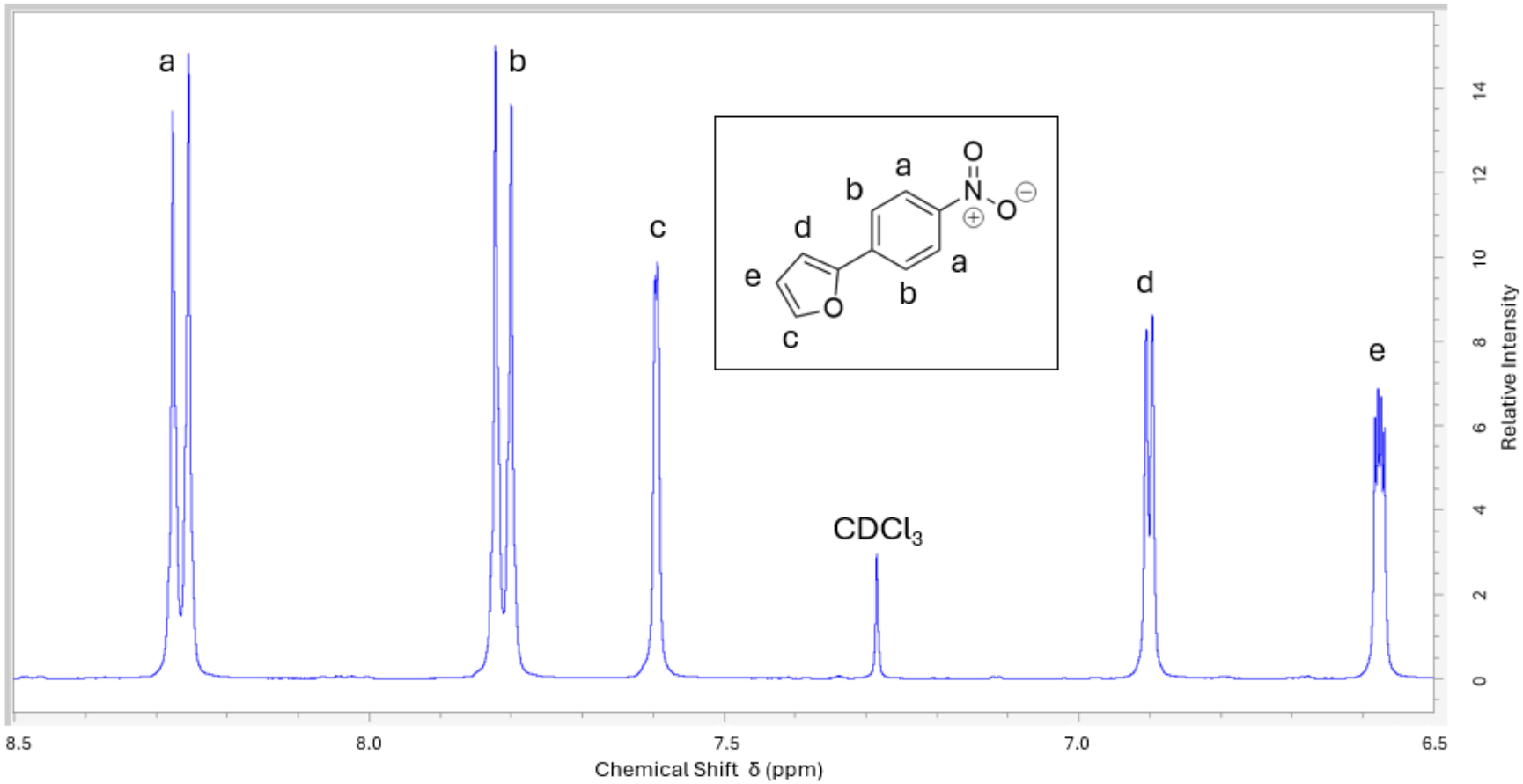

Figure S19: Experimental ^{1}H NMR spectrum of the 2-(4-nitrophenyl) furan product standard (400 MHz, $CDCl_3$). δ ppm 8.24(d, J = 9.0 Hz, 2H), 7.78(d, J = 9.0 Hz, 2H), 7.57(d, J = 1.3 Hz, 1H), 6.87(d, J = 3.3 Hz, 1H), 6.55(dd, J = 3.4, 1.8 Hz, 1H).

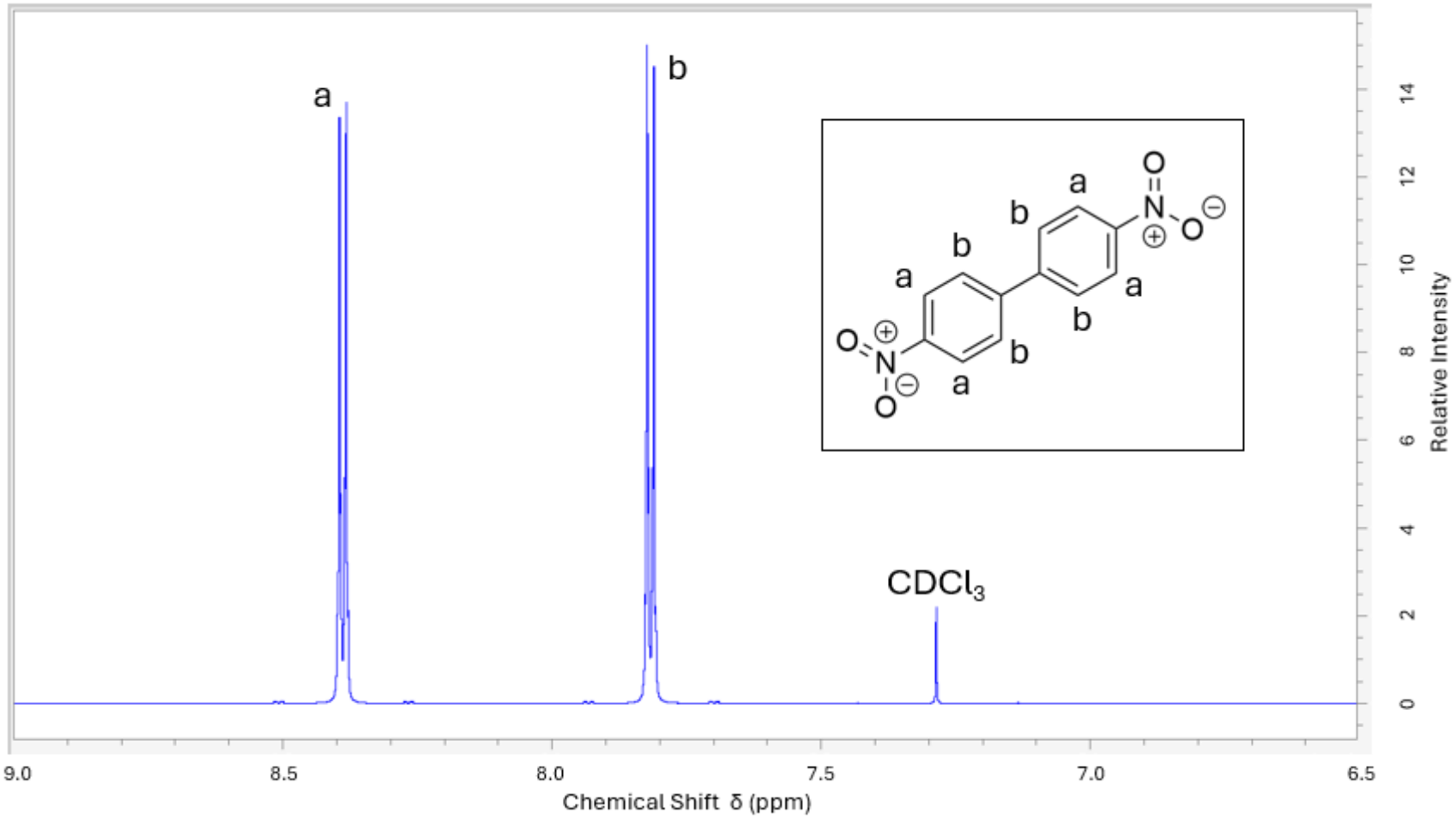

Figure S20: Experimental ^{1}H NMR spectrum of the 4,4'-dinitrobiphenyl dimer product standard (400 MHz, $CDCl_3$). δ ppm 8.34(dd, J = 8.8 Hz, 4H), 7.81(dd, J = 8.8 Hz, 4H).

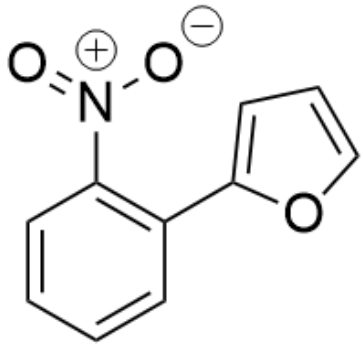

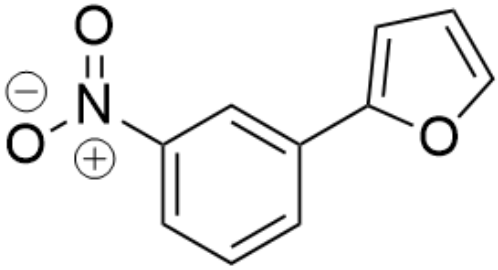

Figure S21: (Left) Ortho 2-(2-nitrophenyl) furan structure. ^{1}H NMR (300 MHz, CDCl3): δ ppm 7.72(dd, J = 7.9, 1.3 Hz, 1H), 7.68(dd, J = 8.1, 1.1 Hz, 1H), 7.57(dt, J = 7.7, 1.3 Hz, 1H), 7.51(d, J = 1.7 Hz, 1H), 7.41(dt, J = 7.8, 1.4 Hz, 1H), 6.67(dd, J = 3.5, 0.4 Hz, 1H), 6.50(dd, J = 3.5, 1.8 Hz, 1H). (Right) Meta 2-(3-nitrophenyl) furan structure. ^{1}H NMR (300 MHz, CDCl3): δ ppm 8.49-8.48(m, 1H), 8.09(ddd, J = 8.2, 2.2, 0.8 Hz, 1H), 7.97-7.94(m, 1H), 7.57-7.51(m, 2H), 6.81(d, J = 3.4 Hz, 1H), 6.53(dd, J = 3.4, 1.8 Hz, 1H).

^{1}H NMR values for the ortho and meta positioned nitrophenyl furan dimers were collected experimentally by Hari et. al.[9] and referenced here to demonstrate that the only product acquired from this arylation reaction was the para positioned nitrophenyl furan depicted in Figure S19.

S2.3 Conversion Metrics

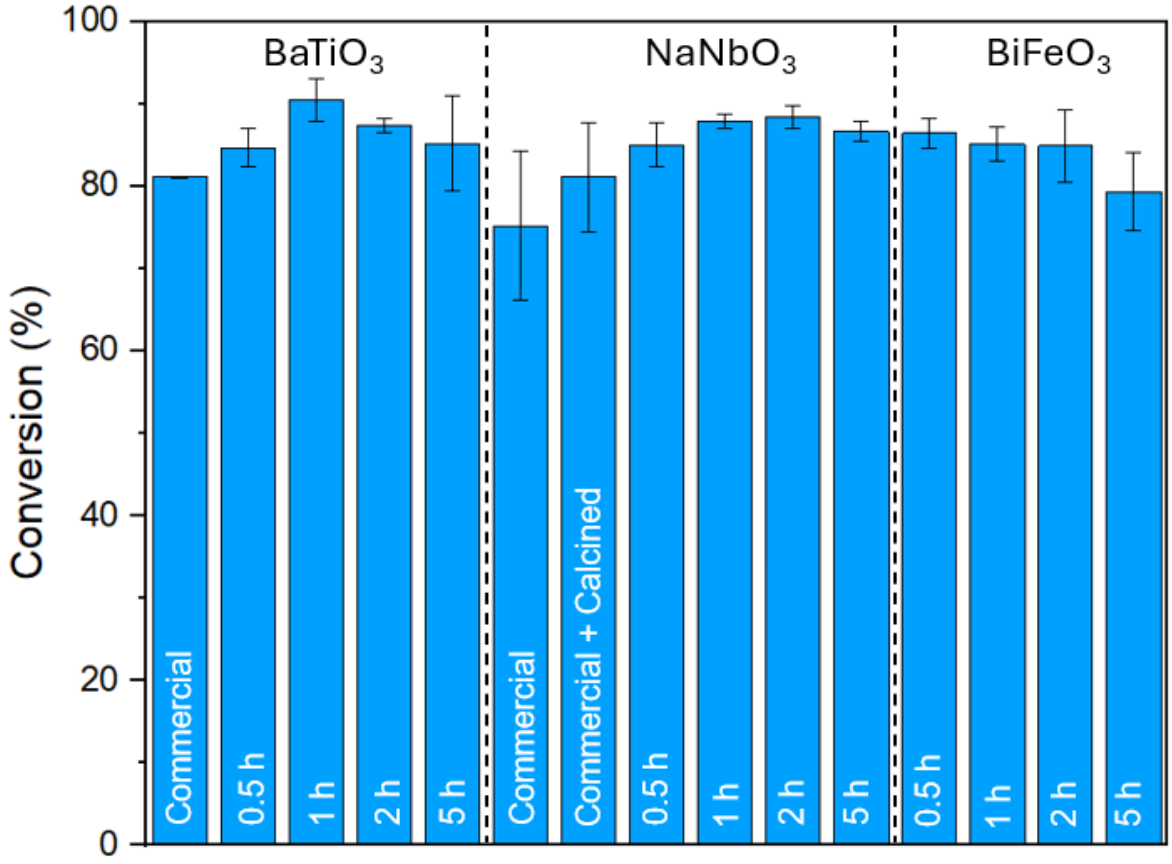

Figure S22: Conversion values and experimental standard deviations for 4-nitrobenzenediazonium tetrafluoroborate after reaction completion using $BaTiO_3$, $NaNbO_3$ and $BiFeO_3$.

The conversion values for this reaction (Figure S22) follow the same general patterns as the yield behavior for $BaTiO_3$, $NaNbO_3$ and $BiFeO_3$ in Figure 6. All conversions fell between 75% to 90%, indicating that 10 – 25% of the salt remained in the vessel after milling was stopped at 60 min. Section 3.3 and 4.2 of the manuscript demonstrated conversion with respect to time for $BaTiO_3$ HM1C, $NaNbO_3$ HM2C and $BiFeO_3$ HM1C; Figure S22 displays the overall conversion and margin of error for the remaining catalysts, in accordance with Figure 6 of the main text.

S2.4 FTIR with ATR Attachment

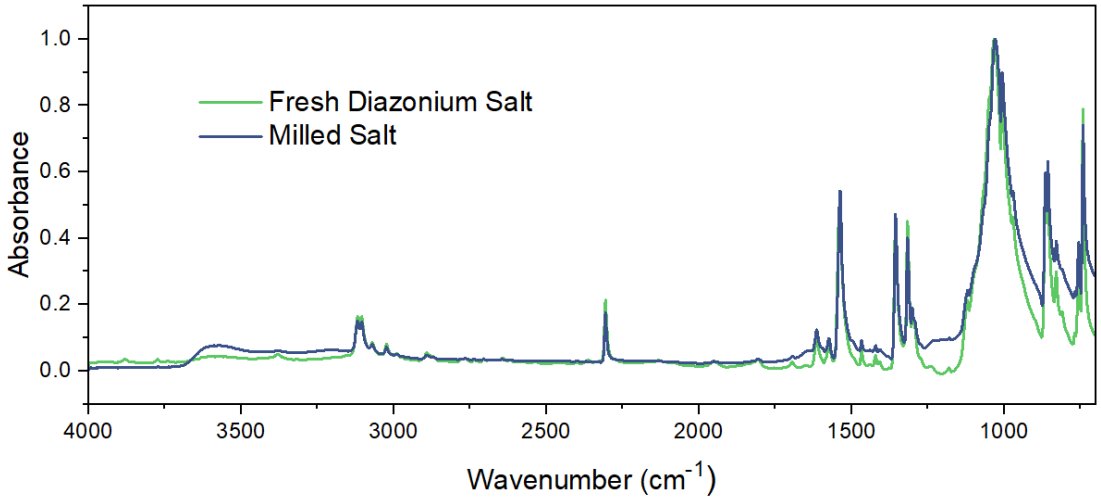

Figure S23: FTIR spectra of 4-nitrobenzenediazonium tetrafluoroborate before and after milling.

For additional characterization, ATR FTIR spectra were measured for the diazonium salt before and after milling for 1 h in a stainless-steel vessel (Figure S23). The results showed that there was strong peak alignment with no new peaks present, with the exception of a broad -OH band present at 3600 cm^{-1}. This was likely due to incorporation of atmospheric moisture throughout sample handling and milling since no purging of the vessel was conducted. The spectra ultimately showed that no other undesirable side reactions occur, and loss of mass balance was due to decomposition of the diazonium salt to gaseous products, as previously mentioned.

References

(1) E. K. Al-Shakarchi, N. B. Mahmood, *J. Mod. Phys.,* 2011, **02**, 1420-1428.

(2) S. Miyake and R. Ueda, *Phys. Soc. Jpn.,* 1947, **2**, 93-97.

(3) C. N. W. Darlington and K. S. Knight, *Acta Cryst.,* 1999, **B55**, 24-30.

(4) S. P. Solov'ev, Y. N. Venevtsev and G. S. Zhdanov, *Kristallografiya.* 1961, **6**, 218.

(5) M. D. Peel, S. P. Thompson, A. Daoud-Aladine, S. E. Ashbrook and P. Lightfoot, *Inorg. Chem.,* 2012, **51**, 6876-6889.

(6) J. M. Moreau, C. Michel, R. Gerson and W. J. James, *J. Phys. Chem. Solids,* 1971, **32**, 1315-1320.

(7) N. Rangavittal, T. N. Guru Row and C. N. R. Rao, In *Advances in Chemistry*, World Scientific Series in 20th Century Chemistry, 2003, 95-108.

(8) N. Niizeki and M. Wachi, *Zeitschrift für Kristallographie - Cryst. Mat.,* 1968, **127**, 173 - 187.

(9) D. P. Hari, P. Schroll and B. Konig, *J. Am. Chem. Soc.,* 2012, **134**, 2958-2961.